High-pressure behavior of $La_xSr_{2-x}MnO_4$ layered manganites investigated by Raman spectroscopy and x-ray diffraction

P. Postorino,[1] A. Congeduti,[1] E. Degiorgi,[2] J.P. Itié,[3] and P. Munsch[3]
[1]*Dipartimento di Fisica, Università di Roma "La Sapienza," Unità dell'Istituto Nazionale per la Fisica della Materia, Piazzale A. Moro 2, 00185 Roma, Italy*
[2]*Dipartimento di Fisica, Università di Tor Vergata, Unità dell'Istituto Nazionale per la Fisica della Materia, Via della Ricerca Scientifica 1, 00133 Roma, Italy*
[3]*Physique des Milieux Condensés, Université Pierre et Marie Curie, B 77, F-75252 Paris, Cedex 05, France*
(Received 18 December 2001; revised manuscript received 7 February 2002; published 22 May 2002)

Raman spectra and x-ray diffraction patterns of $La_{0.5}Sr_{1.5}MnO_4$ and Sr_2MnO_4 layered manganites have been collected over a wide pressure range (0–20 GPa) using a diamond anvil cell. The pressure dependence of both phonon peaks and lattice parameters, as well as the mode-Gruneisen parameters, have been determined. The comparative analysis of the results allows us to give a reliable assignment for the four phonon modes observed in the Raman spectra and in particular to identify the peak at higher frequency as a Jahn–Teller phonon. The comparison between the pressure dependence shown by doped and pure samples evidences the role played by the Jahn–Teller octahedral distortion on the lattice structural and dynamical properties. A progressive pressure-induced reduction of the Jahn–Teller distortion has also been observed in the doped sample. Finally, taking into account of recent results obtained by infrared spectroscopy on high-pressure pseudocubic and layered manganites, the role of lattice dimensionality on the pressure-induced charge delocalization has been discussed.

DOI: 10.1103/PhysRevB.65.224102 PACS number(s): 61.10.Nz, 62.50.+p, 78.30.−j, 75.30.Vn

I. INTRODUCTION

In the last decade a lot of effort has been devoted to investigate the physical properties of the Ruddlesden–Popper series of manganites $A_xA'_{n+1-x}Mn_nO_{3n+1}$ (with A a trivalent rare hearth and A' a divalent metal).[1] Besides their own interest, these compounds have drawn attention as reference systems, enabling a deeper understanding of the phenomena of both high temperature (HT) superconductivity and colossal magnetoresistance (CMR) phenomena. From a structural point of view the single-sheet ($n=1$) layered manganites are isostructural to the $La_xSr_{2-x}CuO_4$ cuprates, the popular family of HT superconductors, and their crystal structure is characterized by a planar arrangement of MnO_6 octahedra, which are also the main building blocks of pseudocubic CMR manganites ($A_{1-x}A'_xMnO_3$).[2,3] In single-sheet layered manganites the octahedra are arranged in a two-dimensional (2D) structure with MnO_6 planes intercalated by planes of A ions while in pseudocubic manganites the A ions are trapped inside a three-dimensional (3D) pseudocubic lattice of octahedra. Noting that the index n in the general formula of the Ruddlesden–Popper series accounts for the number of connected MnO_6 planes, single-sheet and pseudocubic manganites can be taken as the two end-compounds of the series with $n=1$ and $n=\infty$, respectively.[1]

When dealing with doped manganites the manganese ion acquires a mixed valence which can be treated by assuming a coexistence of Mn^{+3} and Mn^{+4} ions in a suitable percentage. Many of the physical properties of these mixed-valence manganites originate from the complex interplay between charge localization, brought about by the Jahn–Teller distortion of the Mn^{+3} centered MnO_6 octahedra, and magnetic interactions (super and double exchange). Transport and magnetic properties of both layered and pseudocubic manganites are thus strongly affected by different *intrinsic* variables (such as the doping concentration, and the average radius r_A of the A and A' ions) and external conditions (temperature, pressure, and applied magnetic field). Such a large number of *degrees of freedom* gives rise, for each manganite, to quite a complex phase diagram, displaying different magnetic phases (ferro-, antiferro-, canted, para-) and metallic (M), insulating (I), and charge ordered (CO) phases.[3–5]

In general, single-layer compounds show an insulating behavior regardless of doping concentration and temperature and, in some systems, a CO transition occurs at low temperatures. On the contrary, in the doping concentration range where CMR occurs, pseudocubic manganites exhibit a metallic phase associated to a ferromagnetic order below the I–M transition temperature T_{IM} (in these systems the Curie temperature T_C is actually coincident with T_{IM}). T_{IM} can be increased by increasing both pressure P and average ionic radius r_A (i.e., $dT_{IM}/dP>0$ and $dT_{IM}/dr_A>0$).[6–9] An intermediate behavior is found in bilayered compounds ($n=2$) with a lower T_{IM} and a less pronounced magnetoresistance than in pseudocubic systems.[1] The occurrence of the metallic phase and of the CMR seems to be related to the crystalline structure which allows for a complete (pseudocubic) or at least a partial (bilayered) caging of the ion at the A site. The basic idea is that both external pressure (P) and *chemical pressure* (r_A) reduce the free volume around the A ion in the cage of the MnO_6 octahedra, thus causing a symmetrization of the surrounding structure with removal of the JT distortion.[6,7,10,11]

Although pressure is an ideal and selective tool for tuning the extent of the JT distortion, few works dealing with manganites in the very high pressure regime (that is P

$>1-2$ GPa) have appeared since now. Raman and structural studies in this high-pressure regime exist for La–Ca pseudocubic manganites both pure[12] and doped,[10,13] while transport properties and structure have been studied in few bilayered compounds.[14–16] In all the mentioned papers a significant pressure-induced reduction of the JT distortion has been directly observed or inferred from the data, although the pseudocubic compound $La_{0.75}Ca_{0.25}MnO_3$ shows the onset of a structural instability around $P^*=7.5$ GPa which seems to inhibit the process.[10,13] To our knowledge the only high-pressure experimental data on a single-sheet layered manganite are those of the infrared measurements over the 0–10 GPa pressure range and focused to study of the pressure-induced charge-delocalization processes in manganites.[11] The result having direct bearing on the present investigation was the weak pressure-induced charge delocalization observed in the single-layer $La_{0.5}Sr_{1.5}MnO_4$, much weaker than the one observed in the pseudocubic $La_{0.75}Ca_{0.25}MnO_3$, at least for $P<P^*$.[11] On the basis of the above discussion, this finding could be ascribed to a reduced efficiency of the external pressure in removing the JT distortion, due to the absence of a caging of the ion at the A site in the layered compound. On the other hand, $La_{0.5}Sr_{1.5}MnO_4$ shows a paramagnetic insulating phase at room temperature and undergoes an antiferromagnetic CO phase down to 220 K, pointing out the relevance of superexchange magnetic interaction.[5,17,18] In $La_{0.5}Sr_{1.5}MnO_4$ the difficulty in delocalizing the charge by pressure could be thus alternatively ascribed to the onset of an incipient pressure-induced CO phase.

In the present paper we have studied two samples of $La_xSr_{2-x}MnO_4$ layered manganite, with $x=0$ and $x=0.5$, by means of x-ray diffraction, over the pressure range 0–20 GPa and Raman spectroscopy, over the pressure range 0–14 GPa. The pure sample Sr_2MnO_4 is characterized by the Mn^{+4} valence only, whereas the doped sample $La_{0.5}Sr_{1.5}MnO_4$ has 50% of Mn^{+3}. Since JT distorted octahedra are present only in the doped sample, the comparison between the pressure behavior exhibited by the two samples will clearly show the effect of the octahedral distortion on both the lattice structure and dynamics. Moreover, the absence of a pressure-driven CO transition will be checked by Raman spectroscopy. As a matter of fact the temperature-driven CO transition is clearly marked by a splitting and a remarkable narrowing of the Raman active phonon lines[19] due to both the reduction of the charge disorder and the lowering of the crystal symmetry. Finally, some conclusions on the relevance of the structure dimensionality on the transport properties of manganites will be drawn by comparing the present results with those previously reported on the pseudocubic $La_{0.75}Ca_{0.25}MnO_3$.[11,13]

II. EXPERIMENT

Characterized polycrystalline samples of doped, $La_{0.5}Sr_{1.5}MnO_4$ (LSMO), and pure, Sr_2MnO_4 (SMO), layered manganites (single sheet, $n=1$)[20,21] have been used for Raman and x-ray experiments. Both the samples have the K_2NiF_4 structure with space group *I4mmm* and one formula unit per primitive cell. Standard membrane diamond anvil cells were used to generate high pressure on the sample. The gaskets were made of a 250 μm thick steel foil. Under working conditions the chamber inside the gasket had a typical diameter of 200 μm and a 30–50 μm height. The anvils used for the Raman measurements were low fluorescence II A diamonds with 800 μm culet diameter, while 600 μm IA diamonds were used for x-ray diffraction. Different pressure transmitting media were used in the two experiments: for optical study the manganite samples were placed at the center of the upper surface of an NaCl pellet presintered at high pressure in the gasket hole while, for x-ray diffraction measurements, finely milled manganite samples were dispersed in silicon oil. Pressure was measured *in situ* by collecting fluorescence spectra from ruby nanospheres placed in the gasket hole, before and after each measurement. We also checked possible pressure gradients and we found that, if any, the pressure differences were within the experimental uncertainty of ± 0.1 GPa. In the Raman measurements the high thermal conductivity of diamond prevented laser-induced sample heating.[10]

Raman spectra were collected in back-scattering geometry, using a LABRAM spectrometer by Dilor with a CCD detector and an adjustable notch filter. The sample was excited by the 632.8 nm line of a 16 mW He–Ne laser. A confocal microscope equipped with a $20\times$ magnification objective was used both to focus the laser beam on the sample and to collect the scattered light. The laser spot at the sample surface was around 10 μm^2. The notch filter cutoff at low frequency and the presence of the very intense diamond Raman peak at high frequency (1330 cm^{-1} at zero pressure) allowed us to collect high-pressure spectra only over the 200–1100 cm^{-1} frequency range. Raman spectra were collected directly from manganite, avoiding any spectral contribution from NaCl and from three different zones of the samples. Data were analyzed separately by a fitting procedure described in the following section and, finally, the best-fit parameters were averaged. The maximum deviation has been assumed as an estimate of the parameter uncertainties.

The high-pressure powder x-ray diffraction measurements were carried out in the energy dispersive mode at LURE synchrotron facility (Orsay, France), using the DCI storage ring on the DW 11 beam line. The white beam was collimated to a 50×50 μm^2 spot, centered on the gasket hole. The diffraction patterns were collected by a Ge detector in the 5–60 keV energy range with a resolution ranging from 150 to 350 eV. The Bragg diffraction angle was set close to 6°. Owing to the high scattering cross section of our samples, exposure times between 20 and 30 minutes were sufficient to collect diffraction patterns with good peak-to-background intensity ratios. No Rietveld refinement of the diffraction patterns has been performed.

III. RAMAN RESULTS

At ambient temperature the crystal structure of both SMO and LSMO belongs to the space group *I4mmm*,[17,18] while a lowering of the crystal symmetry occurs at the CO transition ($T_{CO}=220$ K) in LSMO[17,22]. Using the standard group theory four Raman active modes ($2A_g+2E_g$) can be pre-

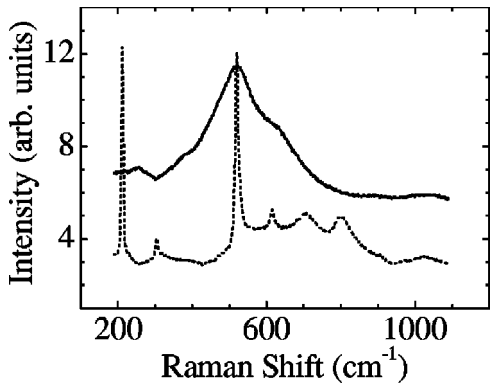

FIG. 1. Raman spectra of SMO (dotted line) and LSMO (solid line) at ambient pressure. LSMO spectrum is offset by about 2.5 units for the sake of clarity.

dicted for the space group *I4mmm*. Only the A-atom and the O_z-atom (out-of-plane oxygen) movements are involved in the Raman active modes: the two high frequency modes involve MnO_6 octahedra [$A_{1g}(1)$ stretching and $E_{1g}(1)$ tilting] while the two low frequency modes involve only the A atoms [$A_{1g}(2)$ and $E_{1g}(2)$].[23]

The ambient pressure Raman spectra of SMO and LSMO polycrystalline samples are shown in Fig. 1. The spectrum of the pure sample in the range of the phonon frequency is characterized by four well defined and narrow peaks around 210 (ν_1^P), 310 (ν_2^P), 520 (ν_3^P), and 615 cm^{-1}(ν_4^P). The two broad structures around 700 and 800 cm^{-1} can be ascribed to combination bands because of their high frequency and large profiles. The same four-peaks structure can be found in the spectrum of the doped sample (LSMO), although in this case the phonon profiles are quite broad, largely overlapped and their positions are slightly shifted [250 (ν_1^D), 380 (ν_2^D), 510 (ν_3^D), 630 cm^{-1} (ν_4^D)]. The huge broadening of the phonon peaks in LSMO is due to the excess charge introduced by La doping which activates the JT distortion in the MnO_6 octahedra and induces, to some extent, lattice disorder. As a matter of fact both electron–phonon interaction (el–ph) and structural disorder cause a reduction of the phonon lifetime, thus widening the peak profiles. This effect, observed also in other strongly correlated systems[24] and in particular in JT systems,[10,25] provides evidence of the strong sensitivity of Raman measurements to the el–ph interaction.

If we assume that the modes responsible for the phonon spectrum are the same in both the LSMO and SMO, the difference in the phonon frequencies could be in principle ascribed to the el–ph interaction (which gives rise to a frequency renormalization) and to the atomic mass factor (La is heavier than Sr). According with the group theory prediction, the two low-frequency phonons should be ascribed to pure A-atoms modes which actually do not depend on the octahedral distortion. Owing to the mass factor, their frequencies are expected to be lower in the La-doped sample (ν_1^D, ν_2^D) than in the pure Sr one (ν_1^P, ν_2^P), in contrast with the present experimental result, which definitively confutes the above assignment. The disagreement with the group theory prediction is not surprising since in disordered or defective strongly correlated system the symmetry selection rules can be violated, and the Raman spectrum can show modes that are forbidden at all or allowed in a different crystal symmetry.[24,26] Unfortunately, the polycrystalline nature of the samples prevented a polarization analysis of the measurements, which could allow the determination of the symmetry of the phonon modes involved.

In any case, some conjectures can be drawn exploiting a quite crude classification which ascribes the modes at high (500–700 cm^{-1}), intermediate (200–500 cm^{-1}), and low (<200 cm^{-1}) frequencies to Mn–O bond stretching, to tilting or rotation of the octahedra and to vibration of the heavy rare earths, respectively.[25,27] The energies involved in ion vibrations are indeed expected to be higher when the strong Mn–O bond is strained than in the case of single A-ion displacements. On the other hand, intermediate energies are expected to be associated to octahedron rigid rotation, which hardly affects the internal octahedral distances, and to the octahedron bending, which in essence involve only O–O bond elongations. Based on these assumptions and exploiting the analogy with Raman measurements on pseudocubic compounds,[28,10] we can tentatively ascribe, in both samples, the two low-frequency modes to a rigid octahedron rotation, while the $\sim$500 cm^{-1} and $\sim$600 cm^{-1} phonons to octahedron bending and stretching (JT) modes, respectively. The temperature dependence of the Raman spectrum of a single crystal of LSMO has been recently investigated at ambient pressure.[19] The room temperature spectrum is in fairly good agreement with the present results and a sharpening of the spectral features occurs when cooling down the sample. In particular, at $T=10$ K (i.e., well below T_{CO}) the Raman spectrum is dominated by very sharp and intense peaks in every investigated polarization configuration. The main features are two peaks around 530 and 630 cm^{-1}, whose assignment, although still controversial, is consistent with our assumptions (notice that the crystal symmetry changes on entering the CO phase).

High-pressure Raman spectra of SMO and LSMO, collected up to 14 GPa by means of the DAC, are shown in panels (a) and (b) of Fig. 2, respectively. The frequency range explored (200–1100 cm^{-1}) allowed us to follow the pressure evolution of the phonon peaks. These are indeed well evident up to the maximum pressure in both the samples, while the two broad structures around 700 and 800 cm^{-1} in the Raman spectrum of SMO, broaden and become less defined as the pressure is increased.

The experimental data have been analyzed by a fitting procedure and damped harmonic oscillators (DHO) have been used for the phonon line shape. The choice of this line profile, successfully employed in fitting broad line shapes in similar systems,[10,25] has been particularly useful in modelling the LSMO experimental data. In the SMO case two couples of DHO functions have been used for separately fitting the two phonon couples ν_1^P–ν_2^P and ν_3^P–ν_4^P. A low-order (1–2) polynomial curve has also been used as a baseline. In the LSMO case, the whole Raman spectrum has been fitted in the 200–900 cm^{-1} frequency range with the following function:

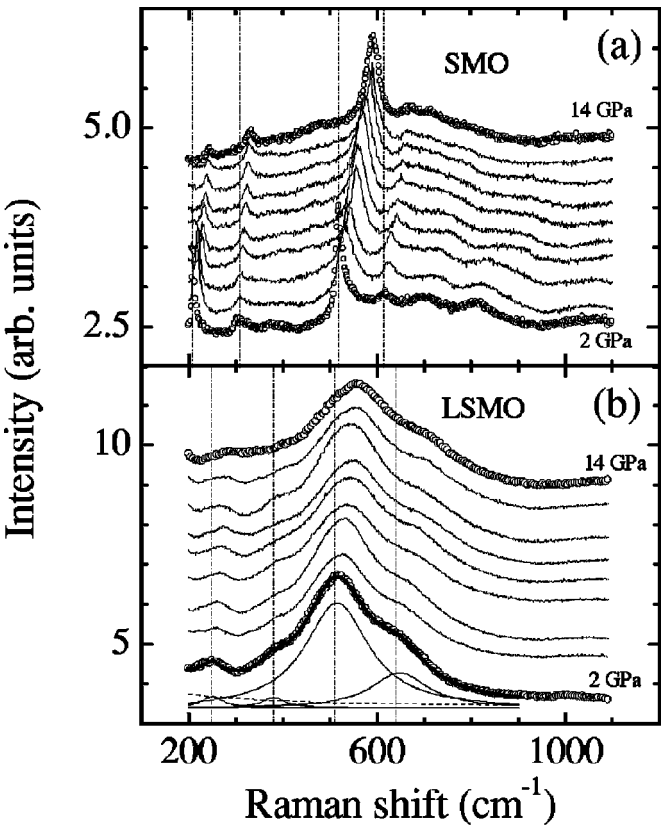

FIG. 2. Raman spectra of SMO (a) and LSMO (b) at different pressures. The pressure increases from ~2 GPa (bottom) to ~14 GPa (top). Successive spectra are offset by a constant (about 0.2 and 0.7 units for SMO and LSMO, respectively) for the sake of clarity. Vertical dashed–dotted lines show the zero-pressure phonon frequencies. In panel (b) the best-fit curve from Eq. (1) is shown by a solid line for the lower-pressure spectrum; the four phonon contributions and the low-frequency carrier hopping contribution (dashed line) are also shown separately.

$$S(\nu)=[1+n(\nu)]\left[\frac{A\nu/\tau}{\nu^2+1/\tau^2}+\sum_{i=1}^{4}\frac{A_i\nu_i^D\Gamma_i}{[\nu^2-(\nu_i^D)^2]^2+\nu^2\Gamma_i^2}\right]. \quad (1)$$

The first term is a large contribution centered at low frequency accounting for the wide unstructured background. This is a common feature of strongly correlated systems such as manganites and cuprates[25] and it is associated with the diffusive hopping of the carriers with a scattering rate $\Gamma=1/\tau$.[29] The second term, a linear combination of four DHO profiles, accounts for the phonon peaks, where ν_i^D, A_i^D, and Γ_i^D are peak frequency, amplitude, and linewidth, respectively (a similar notation, ν_i^P, A_i^P, and Γ_i^P, has been used in the SMO case). The quantity $n(\nu)$ is the Bose–Einstein thermal population factor. The best-fit curves obtained using Eq. (1) are in very good agreement with the experimental data at each pressure. As an example, the best-fit curve and the different component for LSMO at the lowest pressure are also shown in Fig. 2, panel (b).

The best-fit values found for the linewidths in both samples (Γ_i^D and Γ_i^P) show a weak pressure dependence,

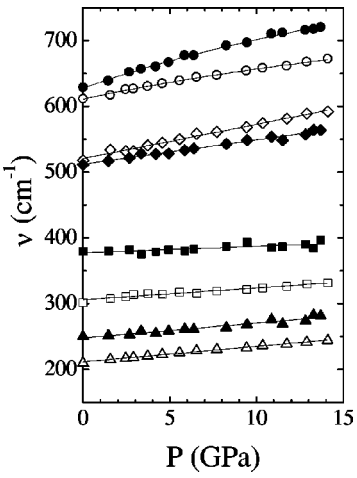

FIG. 3. Pressure dependence of the four phonon peak frequencies: ν_1 (up triangles), ν_2 (squares), ν_3 (diamonds), ν_4 (circles). Open and solid symbols refer to the SMO and LSMO samples, respectively. The error bars are of the same order of magnitude as the symbol size. The solid lines represent the best-fit curves obtained by Eq. (2).

namely they slightly increase under pressure (about 10–20% over the 0–14 GPa pressure range). It is worth to notice that this effect can be partially ascribed to the onset of unavoidable anisotropic stress under pressure and that, in any case, a proper analysis of the pressure dependence of these values can be hardly carried out due to their large uncertainties (the Γ_i parameters show the highest degree of correlation). Besides the previously discussed well apparent broadening of the peaks in LSMO with respect to SMO, it is interesting to note that Γ_3^D and Γ_4^D are much larger than Γ_1^D and Γ_2^D (≈ 150 cm^{-1} vs ≈ 50 cm^{-1} at ambient pressure, respectively) which, in turn, are close to the average value of the Γ_i^P. Such a large difference is consistent with the proposed assignment of the phonon peaks: the two high frequency modes indeed involve strain of the octahedral structure and thus they are more coupled to the JT distortion.

No systematic pressure dependence of either the overall Raman signal or the single mode amplitude A_i was observed. We want to point out that the absolute intensities of the Raman modes can be affected by both different focusing and average orientation of the microcrystals impinged by the laser beam.

The best-fit values of ν_i are shown in Fig. 3 as a function of pressure for both the samples. All phonon frequencies show a regular and almost linear pressure-induced hardening. The two high frequency modes (ν_3 and ν_4) exhibit a rate of increase much larger than the other ones and in particular ν_4^D shows the largest rate. The latter finding and the occurrence of the largest difference in the pressure behavior between corresponding modes in the two samples for ν_4, are further indications of the JT nature of this mode.

A weak sublinear dependence on pressure can be observed in the ν_4 mode frequencies and the results have been analyzed assuming a pressure dependence given by the widely used relation

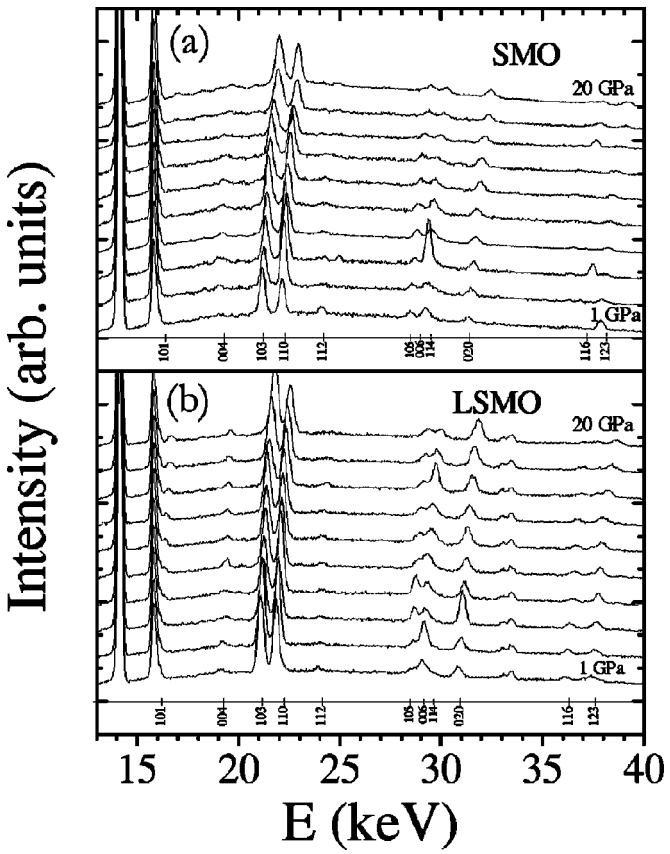

FIG. 4. X-ray diffraction patterns collected at different pressures on SMO (a) and on LSMO (b). The pressure increases from 1 GPa (bottom) to 20 GPa (top). The assignment of the main Bragg peaks are also reported.

$$\nu_i(P)/\nu_i^0=[(\delta_i^0/\delta_i')P+1]^{\delta_i'}, \tag{2}$$

where ν_i^0, δ_i^0, and δ_i' are taken as free fitting parameters. It is worth to notice that ν_i^0 represent the zero pressure frequency value of the ith mode and δ_i^0 is its logarithmic pressure derivative $(d \ln \nu_i/dP)_{P=0}$. A simple linear fit (i.e., fixing δ_i' to 1) has been adopted for all the other modes. The best-fit values obtained for ν_i^0, δ_i^0, and δ_i' $(i=4)$ for SMO and LSMO are reported in Table 1. The best-fit curves are also shown in Fig. 3.

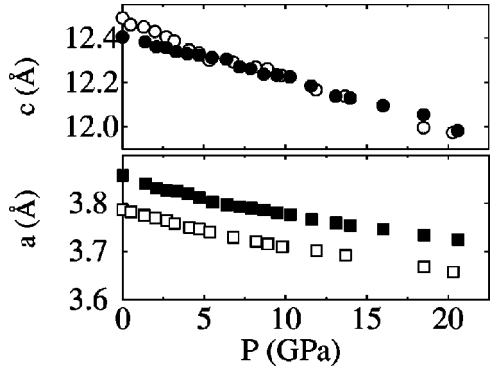

FIG. 5. Pressure dependence of the a (squares) and c (circles) lattice parameters. Open and solid symbols refer to the SMO and LSMO samples, respectively. The error bars are of the same order of magnitude as the symbol size.

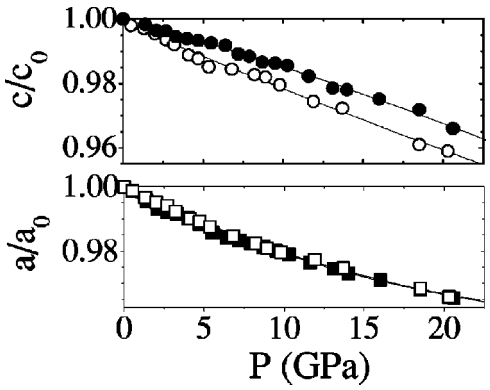

FIG. 6. Pressure dependence of the a/a_0 (lower panel) and the c/c_0 (upper panel) ratios. a_0 and c_0 are the lattice parameter values at zero pressure. Open and solid symbols refer to the SMO and LSMO samples, respectively. The error bars are of the same order of magnitude as the symbol size. The solid lines are guides for the eyes.

IV. X-RAY DIFFRACTION RESULTS

X-ray diffraction measurements have been performed on SMO and LSMO samples over the 0–20 GPa pressure range. Diffraction patterns collected at different pressures are shown in Fig. 4 for SMO [panel (a)] and LSMO [panel (b)], respectively. The assignment of the main Bragg peaks is reported in the same figure. The fluctuations in the Bragg peak intensities (see, for example, the Bragg peaks around 30 keV in the figure) have to be mainly ascribed to pressure-induced rearrangements of the grains of sample powder. Indeed, although the sample was finely milled before loading, it is very easy for preferred orientations to occur since the dimensions of the gasket hole limits the quantity of samples to very small amount only.

We analyzed the data by means of a fitting procedure to

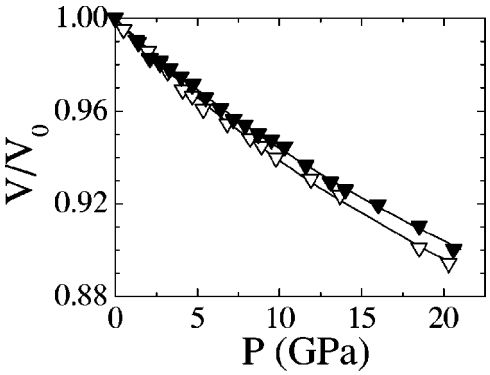

FIG. 7. Pressure dependence of the free volume V/V_0, where V_0 is the unit cell volume at zero pressure. Open and solid symbols refer to the SMO and LSMO samples, respectively. The error bars are of the same order of magnitude as the symbol size. The solid lines represent the Birch–Murnaghan best-fit curves obtained by Eq. (3).

TABLE I. Best-fit values, obtained using Eq. (2), and Gruneisen parameters for the four phonon modes of SMO and LSMO.

Mode	$\nu^0(\mathrm{cm}^{-1})$	$\delta^0(\mathrm{GPa}^{-1})$	δ'	γ_0
(SMO) ν_1^P	212	0.011	1 fix.	1.4
(SMO) ν_2^P	306	0.006	1 fix.	0.8
(SMO) ν_3^P	521	0.016	1 fix.	2.1
(SMO) ν_4^P	611	0.0095	0.14	1.2
(LSMO) ν_1^D	248	0.0092	1 fix.	1.3
(LSMO) ν_2^D	377	0.0026	1 fix.	0.4
(LSMO) ν_3^D	512	0.0072	1 fix.	1.0
(LSMO) ν_4^D	627	0.015	0.18	2.2

refine the *a* and *c* lattice parameters of the tetragonal structure of the layered manganites. The energy range explored allows to follow the evolution of 11 Bragg peaks. The whole diffraction pattern was fitted using a smooth background and 11 Gaussian profiles. Exploiting the Bragg condition, all the energies at which the Gaussian profiles are centered have been expressed as a function of the two lattice parameters and the scattering angle only. The values obtained for the *a* and *c* lattice parameters are shown in Fig. 5 as a function of pressure. The zero pressure values are in good agreement with those reported in the literature.[18] From the comparison between the refined parameters of the pure and the doped samples, two main differences can be evidenced: the doped LSMO sample shows a slightly lower distance between the plane of MnO_6 octahedra in the low pressure region (see the *c* lattice parameter in Fig. 5) and a larger *a* parameter than the pure SMO sample. The former difference could be ascribed to a simple steric effect due to slightly larger ionic radius of Sr with respect to that of La [$r_{\mathrm{Sr}}=1.31$ Å, $r_{\mathrm{La}}=1.216$ Å (Ref. 30)] while the latter has to be discussed in terms of charge-lattice interaction. The charge in excess introduced by doping, indeed, activate the JT lattice distortion expanding the *a* parameter in the doped LSMO. In Fig. 6 the a/a_0 and the c/c_0 pressure behavior is shown for both samples (a_0 and c_0 are the lattice parameters at zero pressure). We can notice that the rate of contraction of the *a* parameter (i.e. of the plane of the octahedra) is the same in both the samples while a larger contraction occurs in the pure sample for the *c* parameter (i.e., the distance between the octahedra planes).

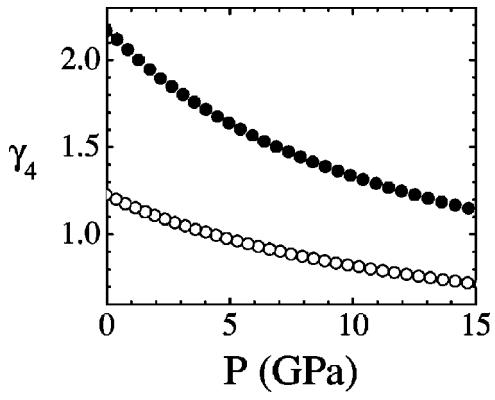

FIG. 8. Pressure dependence of the γ_4 JT mode-Gruneisen parameter. Open and solid symbols refer to the SMO and LSMO samples, respectively.

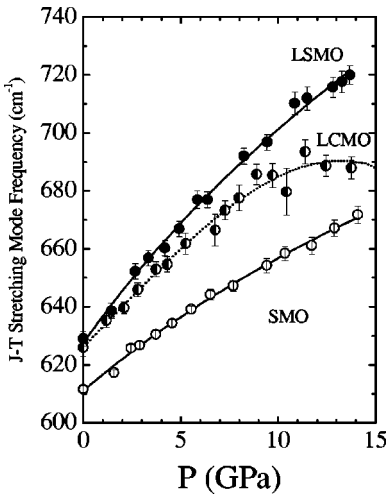

FIG. 9. Pressure dependence of the JT stretching-mode frequency: LCMO from Ref. 10 (half-filled symbols), LSMO and SMO from the present experiment (solid and open symbols, respectively). The solid lines are the best-fit curves obtained by Eq. (2); the dotted line is a guide for the eyes.

In Fig. 7 the pressure dependence of the free volume, $\eta = V/V_0$, is shown for the two samples. The pressure dependence of our data can be well described by a Birch–Murnaghan curve:[31–33]

$$P=\tfrac{3}{2}K_0[\,\eta^{-\frac{7}{3}}-\eta^{-\frac{5}{3}}]\{1+\tfrac{3}{4}(K'-4)[\,\eta^{-\frac{2}{3}}-1]\}, \quad (3)$$

where K_0 the bulk modulus and K' its pressure derivative. The best-fit curves obtained using Eq. (3) are in good agreement with the experimental results as shown in Fig. 7. The best-fit values are $K_0^P=129$ GPa and $K'=6.3$ for SMO and $K_0^D=144$ GPa and $K'=6.3$ for LSMO. These values are comparable with those typically obtained for other perovskites[13] and the comparison shows a 10% increase of steepness for LSMO sample.

Using the phonon frequencies shown in Fig. 3 and the structural parameters shown in Fig. 5, we finally calculate the mode-Gruneisen parameter values given by

$$\gamma_i=-\frac{\partial\ln(\nu_i)}{\partial\ln(V)}=-\left(\frac{1}{\nu_i}\frac{\partial\nu_i}{\partial P}\right)\Big/\left(\frac{1}{V}\frac{\partial V}{\partial P}\right). \quad (4)$$

From Eq. (4) the zero pressure mode-Gruneisen parameters γ_i^0 can be simply obtained by $\gamma_i^0=\delta_i^0 K_0$ since $\delta_i^0=1/\nu_i^0\cdot(d\nu_i/dP)|_{P=0}$ and $1/K_0=1/V_0\cdot(dV/dP)|_{P=0}$ follow from Eq. (2) and Eq. (3), respectively. The zero pressure mode-Gruneisen parameter values are reported in Table I for all the phonon modes and both the samples.

A weak pressure dependence of the γ values has been found in the 0–15 GPa pressure range for every mode a part from the JT mode of the doped sample, which is shown in Fig. 8 in comparison with the analogous mode in the SMO

sample. The variation in this case is dramatic, from the quite high value of 2.2 at $P=0$ it rapidly dropped to 1.2 at $P=15$ GPa.

V. DISCUSSION AND CONCLUSIONS

As a first remark, the present results show that no dramatic changes of any of the measured quantities occur, thus indicating that no CO transition is induced by pressure in the explored range. This finding is in agreement with the results of a previous high-pressure infrared study:[11] these systems show indeed a quite stable behavior under pressure, differently to what is shown by pseudocubic systems.[10,12]

To our knowledge, no experimental data under pressure in the high pressure regime on single layered manganites, but ours in Ref. 11, have been published so far, while several studies have been reported on bilayered doped compounds ($n=2$ in the Ruddlesden–Popper series).[14–16] In particular an almost linear pressure dependence of the *a* and *c* lattice parameters has been found for $La_{1.2}Sr_{1.8}Mn_2O_7$ (up to ~1 GPa, Ref. 14) and $(La_{0.6}Nd_{0.4})_{1.2}Sr_{1.8}Mn_2O_7$, (up to ~9 GPa, Ref. 16). In both cases the compressibility along the *a* axis is about 1.5 times larger than along the *c* axis. In the present experiment this behavior is shown only by the LSMO sample, whereas SMO exhibits an almost isotropic compression (see Fig. 6), thus suggesting the relevance of the doping activated JT distortion. Within a linear approximation, an estimate of the compressibility along the *a* and *c* axes $[\beta_a=-(\partial/\partial P)(a/a_0)$ and $\beta_c=-(\partial/\partial P)(c/c_0)$, respectively] yields indeed $\beta_a^P \simeq \beta_a^D \simeq 2.2\times10^{-3}$ GPa^{-1}, $\beta_c^P \simeq 2.2\times10^{-3}$ GPa^{-1}, and $\beta_c^D \simeq 1.5\times10^{-3}$ GPa^{-1} in the 0–10 GPa pressure range. Although the *softness* of the octahedral plane with respect to the interlayer axes could be expected in doped compounds, it is interesting to note that this order is restored in LSMO not by an increase in compressibility along the *a* axis, but by an *hardening* along the *c* axis. This effect can be explained by taking into account that the metric in-plane JT distortion can be allocated along the MnO_6 plane by a buckling of the distorted octahedra. As a consequence, the interplane distance can get shorter with the hardening of the lattice along the *c* axis.

The different pressure behavior of the octahedron bending phonons ν_3 in the two samples (see Table I and Fig. 3) can be explained by the different contraction of the *c* axis, whereas the pressure behavior of the ν_4^D and ν_4^P modes, shown in more detail in Fig. 9, involves directly the electronic properties of the systems. As is well evident from the figure, the phonon frequency of LSMO shows a quite remarkable pressure dependence in comparison with that of SMO. The observed difference must be ascribed to the strong doping-activated charge-lattice interaction, since the almost identical pressure dependence of the *a* axis in both the compounds (see Fig. 6) suggests the weak relevance of steric effects. Indeed the progressive pressure-induced removal of the JT distortion gives a further contribution to the *natural* hardening of the ν_4^D frequency due to the Mn–O bond contraction.

When the JT effect is turned on by doping, a further contribution on the mode anharmonicity is also expected. Since the mode-Gruneisen parameter is a measure of the extent of the mode anharmonicity, the signature of this effect is shown in Fig. 8. In agreement with the idea of a pressure-induced reduction of the JT distortion,[3,7] the large anharmonicity of the ν_4^D mode, shown by the relatively large value of its mode-Gruneisen parameter at ambient pressure, decreases with increasing pressure as pointed out by the remarkable reduction of $\gamma_4^D(P)$.

Finally, we would like to compare the present results on LSMO with those obtained on the high-pressure pseudocubic manganite $La_{0.75}Ca_{0.25}MnO_3$[10,11] (referred as LCMO in the following). For the sake of comparison the pressure behavior of the JT mode in LCMO[10] is also shown in Fig. 9. In agreement with the above discussion it is well evident that a much stronger pressure dependence of the JT modes is shown by the two doped compounds in comparison with the pure one. Moreover in the 0–7 GPa pressure range, almost identical frequency values and pressure dependence are shown by the JT phonons of the doped compounds, whereas a quite stronger extent of charge delocalization was observed in LCMO than in LSMO.[11] The strong similarity of the phonon behavior observed, at least before the onset of the structural instability in LCMO, confirms the common nature of the vibrational modes involved. On the contrary, in order to explain the different extent of pressure-induced charge delocalization, we have to take into account the different dimensionality of the octahedral arrangement, which is 2D for LSMO and 3D for LCMO. The number of first neighboring octahedra is 4 in the 2D lattice while 6 in the 3D one. As a consequence, the average number of distorted MnO_6 units within the cage of the first neighboring octahedra is approximately 2 in LSMO (50% of Mn^{+3}) and 5 in LCMO (75% of Mn^{+3}). The above differences and the possibility of buckling of the octahedra in the layered compound enable to place JT distorted octahedra in the 2D square lattice of LSMO more easily than in the 3D cubic lattice of LCMO. In other words, the dimension of the structural perturbation of the lattice of the octahedra around a given distorted octahedron (i.e., around a Mn^{+3} ion) is smaller in LSMO than in LCMO. In a polaronic scenario the dimension of the lattice perturbation associated with charge is directly proportional to the polaron mobility,[34] i.e., the larger the dimension the higher the polaron mobility. In the layered compound we have a charge self-trapped in small local lattice distortion which can be hardly affected by pressure while on the contrary the large extension of the lattice distortion in the pseudocubic system allow an easier pressure induced charge delocalization. The pressure is thus much more effective in delocalizing charge (i.e., polaron) in LCMO than in LSMO, although a similar reduction of the JT octahedral distortion is suggested in both the compounds by the similar pressure dependence of the JT phonons.

In conclusion, the present data represent an experimental investigation of the physical properties of single-sheet layered manganites carried out over a wide pressure range. Pressure dependence of both phonon peaks and lattice parameters have been obtained in $La_{0.5}Sr_{1.5}MnO_4$ and Sr_2MnO_4. The comparative analysis of the results allows to identify the peak at higher frequency in the Raman spectrum as a JT

phonon and to give a reliable assignment for the other three phonon modes observed. The relevance of the JT octahedral distortion on the lattice structural and dynamic properties has been highlighted by comparing the pressure dependence shown by doped and pure samples. This analysis, supported by the strong pressure dependence exhibited by the mode-Gruneisen parameter of the J-T phonon in the doped sample, shows a progressive pressure-induced reduction of the JT distortion. Finally, in comparing the present results with those obtained in previous infrared and Raman high-pressure investigations of a pseudocubic manganite, the role played by the lattice dimensionality (3D vs 2D) on the pressure-induced charge delocalization mechanism is evidenced.

ACKNOWLEDGMENTS

We would like to acknowledge Professor M. Nardone for helpful support and fruitful discussions during the Raman experiment.

[1] Y. Moritomo, A. Asamitsu, H. Kuwahara, and Y. Tokura, Nature (London) **380**, 141 (1996).
[2] A.J. Millis, Nature (London) **392**, 147 (1998).
[3] S-W. Cheong and H.Y. Hwang, in *Colossal Magneto Resistance Oxides. Monograph in Condensed Matter Science*, edited by Y. Tokura (Gordon & Branch, New York, 2000).
[4] A. Moreo, S. Yunoki, and E. Dagotto, Science **283**, 2034 (1999).
[5] Y. Moritomo, Y. Tomioka, A. Asamitsu, Y. Tokura, and Y. Matsui, Phys. Rev. B **51**, 3297 (1995).
[6] V. Laukhin, J. Fontcuberta, J.L. Garcia-Muñoz, X. Obradors, Phys. Rev. B **56**, R10 009 (1997); J. Foncuberta, V. Laukhin, and X. Obradors, Appl. Phys. Lett. **72**, 2607 (1998).
[7] H.Y. Hwang, T.T.M. Palstra, S-W. Cheong, and B. Batlogg, Phys. Rev. B **52**, 15 046 (1995).
[8] J.J. Neumeier, M.F. Hundley, J.D. Thompson, and R.H. Heffner, Phys. Rev. B **52**, R7006 (1995).
[9] Y.S. Wang, A.K. Heilman, B. Lorenz, Y.Y. Xue, and C.W. Chu, J.P. Franck, and W.M. Chen, Phys. Rev. B **60**, R14 998 (1999).
[10] A. Congeduti, P. Postorino, E. Caramagno, M. Nardone, A. Kumar, and D.D. Sarma, Phys. Rev. Lett. **86**, 1251 (2001).
[11] A. Congeduti, P. Postorino, P. Dore, A. Nucara, S. Lupi, S. Mercone, P. Calvani, A. Kumar, and D.D. Sarma, Phys. Rev. B **63**, 184410 (2001).
[12] I. Loa, P. Adler, A. Grzechnik, K. Syassen, U. Schwarz, M. Hanfland, G.K. Rozenberg, P. Gorodetsky, and M.P. Pasternak, Phys. Rev. Lett. **87**, 125501 (2001).
[13] C. Meneghini, D. Levy, S. Mobilio, M. Ortolani, M. Nũnez-Reguero, A. Kumar, and D.D. Sarma, Phys. Rev. B **65**, 012111 (2001).
[14] D.N. Argyriou, J.F. Mitchell, J.B. Goodenough, O. Chmaissem, S. Short, and J.D. Jorgensen, Phys. Rev. Lett. **78**, 1568 (1997).
[15] T. Kimura, A. Asamitsu, Y. Tomioka, and Y. Tokura, Phys. Rev. Lett. **79**, 3720 (1997).
[16] K.V. Kamenev, M.R. Lees, G. Balakrishnan, D.M. Paul, W.G. Marshall, V.G. Tissen, and M.V. Nefedova, Phys. Rev. Lett. **84**, 2710 (2000).
[17] B.J. Sternlieb, J.P. Hill, U.C. Wildgruber, G.M. Luke, B. Nachumi, Y. Moritomo, and Y. Tokura, Phys. Rev. Lett. **76**, 2169 (1996).
[18] W. Bao, C.H. Chen, S.A. Carter, and S-W. Cheong, Solid State Commun. **98**, 55 (1996).
[19] K. Yamamoto, T. Kimura, T. Ishikawa, T. Katsufuji, and Y. Tokura, Phys. Rev. B **61**, 14 706 (2000).
[20] P. Calvani, A. Paolone, P. Dore, S. Lupi, P. Maselli, P.G. Medaglia, and S-W. Cheong, Phys. Rev. B **54**, R9592 (1996).
[21] A. Paolone, P. Giura, P. Calvani, P. Dore, S. Lupi, and P. Maselli, Physica B **244**, 33 (1998).
[22] Priya Mahadevan, K. Terakura, and D.D. Sarma, Phys. Rev. Lett. **87**, 066404 (2001).
[23] L. Pintschovius, J.M. Bassat, P. Odier, F. Gervais, G. Chevrier, W. Reichardt, and F. Gompf, Phys. Rev. B **40**, 2229 (1989).
[24] P. Postorino, A. Congeduti, P. Dore, A. Nucara, D. DiCastro, A. Bianconi, S. De Negri, and A. Saccone, Phys. Rev. B **65**, 020507(R) (2002).
[25] S. Yoon, H.L. Liu, G. Schollerer, S.L. Cooper, P.D. Han, D.A. Payne, S-W. Cheong, and Z. Fisk, Phys. Rev. B **58**, 2795 (1998).
[26] G.A. Kourouklis, A. Jayaraman, W. Weber, J.P. Remeika, G.P. Espinosa, A.S. Cooper, R.G. Maines, Sr., Phys. Rev. B **36**, 7218 (1987); A.I. Maksimow, O.V. Misochko, I.T. Tartakovsky, V.B. Timofeev, J.P. Remeika, A.S. Cooper, and Z. Fisk, Solid State Commun. **66**, 1077 (1988).
[27] M.V. Abrashev, V.G. Ivanov, M.N. Iliev, R.A. Chakalov, R.I. Chakalova, and C. Thomsen, Phys. Status Solidi B **215**, 631 (1999).
[28] M.N. Iliev, M.V. Abrashev, H.G. Lee, V.N. Popov, Y.Y. Sun, C. Thomsen, R.L. Meng, and C.W. Chu, Phys. Rev. B **57**, 2872 (1998).
[29] T. Katsufuji and Y. Tokura, Phys. Rev. B **49**, 4372 (1994).
[30] R.D. Shannon, Acta Crystallogr., Sect. A: Cryst. Phys., Diffr., Theor. Gen. Crystallogr. **32**, 751 (1976).
[31] F. Birch, Phys. Rev. **71**, 809 (1947).
[32] O.L. Anderson, *Equations of State of Solids for Geophysics and Ceramic Science* (Oxford University Press, New York, 1995).
[33] O. Schulte and W.B. Holzapfel, Phys. Rev. B **53**, 569 (1996).
[34] P. Calvani, Nuovo Cimento Soc. Ital. Fis., C **24**, 1 (2001); Y. Okimoto, T. Katsufuji, T. Ishikawa, T. Arima, and Y. Tokura, Phys. Rev. B **55**, 4206 (1997); K.H. Kim, J.H. Jung, and T.W. Noh, Phys. Rev. Lett. **81**, 1517 (1998).